

See discussions, stats, and author profiles for this publication at: <https://www.researchgate.net/publication/6923274>

Ultrafast Dynamics of Self-Assembled Monolayers under Shock Compression: Effects of Molecular and Substrate Structure

ARTICLE *in* THE JOURNAL OF PHYSICAL CHEMISTRY B · MARCH 2005

Impact Factor: 3.3 · DOI: 10.1021/jp0450742 · Source: PubMed

CITATIONS

26

READS

21

4 AUTHORS, INCLUDING:



Alexei Lagutchev

Purdue University

44 PUBLICATIONS 719 CITATIONS

SEE PROFILE



Wentao Huang

University of Colorado Boulder

58 PUBLICATIONS 585 CITATIONS

SEE PROFILE



Dana D Dlott

University of Illinois, Urbana-Champaign

297 PUBLICATIONS 6,632 CITATIONS

SEE PROFILE

Ultrafast Dynamics of Self-Assembled Monolayers under Shock Compression: Effects of Molecular and Substrate Structure

Alexei S. Lagutchev, James E. Patterson,[†] Wentao Huang, and Dana D. Dlott*

School of Chemical Sciences, University of Illinois at Urbana–Champaign, Box 01-6 CLSL,
600 South Mathews Avenue, Urbana, Illinois 61801

Received: October 28, 2004; In Final Form: December 21, 2004

Laser-driven ~ 1 GPa shock waves are used to dynamically compress self-assembled monolayers (SAMs) consisting of octadecanethiol (ODT) on Au and Ag, and pentadecanethiol (PDT) and benzyl mercaptan (BMT) on Au. The SAM response to <4 ps shock loading and ~ 25 ps shock unloading is monitored by vibrational sum-frequency generation spectroscopy (SFG), which is sensitive to the instantaneous tilt angle of the SAM terminal group relative to the surface normal. Arrival of the shock front causes SFG signal loss in all SAMs with a material time constant <3.5 ps. Thermal desorption and shock recovery experiments show that SAMs remain adsorbed on the substrate, so signal loss is attributed to shock tilting of the methyl or phenyl groups to angles near 90° . When the shock unloads, PDT/Au returns elastically to its native structure whereas ODT/Au does not. ODT evidences a complicated viscoelastic response that arises from at least two conformers, one that remains kinetically trapped in a large-tilt-angle conformation for times >250 ps and one that relaxes in ~ 30 ps to a nearly upright conformation. Although the shock responses of PDT/Au, ODT/Ag, and BMT/Au are primarily elastic, a small portion of the molecules, 10–20%, evidence viscoelastic response, either becoming kinetically trapped in large-tilt states or by relaxing in ~ 30 ps back to the native structure. The implications of the observed large-amplitude monolayer dynamics for lubrication under extreme conditions of high strain rates are discussed briefly.

1. Introduction

In this paper, we report time-resolved spectroscopy studies of shock-induced ultrafast large-amplitude molecular deformation¹ of self-assembled monolayers (SAMs),² using a combination^{3,4} of femtosecond laser-generated shock compression and vibrational sum-frequency generation (SFG) spectroscopy.^{5,6} In the second paper of this series⁷ we will use molecular simulations to provide a molecular picture of this shock compression and unloading process.

Here we will compare the response of SAMs⁸ on evaporated polycrystalline (111) Au or Ag substrates,⁹ formed from long-chain alkanes with either an even (18) or odd (15) number of carbon atoms thereby having many conformational degrees of freedom, or a short-chain aromatic SAM with minimal degrees of freedom. These materials are octadecanethiol (ODT, $\text{CH}_3-(\text{CH}_2)_{17}-\text{SH}$), pentadecanethiol (PDT, $\text{CH}_3-(\text{CH}_2)_{14}-\text{SH}$), and benzyl mercaptan (BMT, $\text{C}_6\text{H}_5-\text{CH}_2-\text{SH}$).

The shock waves used here produce planar uniaxial compression (loading) with <4 ps rise times, followed by a return (unloading) to ambient pressure in tens of picoseconds. The peak pressure is estimated to be ~ 1 GPa, which is expected to give a volume compression factor $\Delta V = (V_i - V_f)/V_i \approx 10\%$. Thus for a 15- or 18-carbon chain, this shock compression process temporarily shortens the chains by an amount equivalent to one or two carbon units. The SFG probe in the C–H stretching region allows a real-time determination of the instantaneous orientation of the ODT and PDT terminal methyl groups¹⁰ and

the BMT phenyl group. With SFG we can determine if the SAM response to shock is primarily elastic or viscoelastic,¹¹ and we can determine time constants^{12,13} associated with shear relaxation from highly deformed configurations.

High-speed molecular dynamics are more commonly studied by ultrafast laser pump–probe techniques. These techniques are useful for processes that can be photoinitiated, such as photodissociation, photoisomerization or solvation.¹⁴ However, many interesting processes cannot be triggered by photon absorption. By converting photons into shock waves, one can study large-amplitude molecular motions^{1,15} relevant to high-wear tribology, lubrication at rapidly moving metal surfaces, high-speed projectile impacts, biological tissue dynamics during pulsed laser surgeries, and detonation of high explosives.

One important difference between laser pump–probe and shock pump/optical probe techniques^{1,3,16,17} is the velocity mismatch between pump and probe. In a laser pump–probe experiment, both pump and probe pulses transit the sample at the same approximate velocity, so the time resolution is generally limited by the pulse duration alone (neglecting dispersion effects that might degrade the time resolution in thicker samples). Shock waves in condensed matter travel $\sim 10^5$ times slower than light, at velocities of several km/s, or several nm/ps. An optical probe pulse transits a sample layer comparatively instantaneously, but the time needed for a shock to compress a sample layer is equal to the shock front transit time across the sample layer. Thus in shock experiments with steeply rising shock fronts, the time resolution is most often limited by the shock transit time. To obtain time resolution of, e.g., 1 ps, in a shock experiment the layer being probed should not exceed¹ a few nanometers (tens of atomic diameters) in effective thickness. The effective thickness is either the actual layer

* Corresponding author. E-mail: dlott@scs.uiuc.edu. Ph: (217) 333-3574.

[†] Present address, Institute for Shock Physics, Washington State University, Pullman, WA 99164-2816.

thickness for optically thin layers or the optical penetration depth for optically thick layers. The highest depth resolution of a shock front attained so far has been achieved with visible or near-IR probing of reflective metal surfaces,¹⁸ where the optical penetration depth is ~ 5 nm, or about 50 atomic diameters. For molecular dielectrics which typically have optical penetration depths > 1 μm , the highest depth resolution obtained prior to our^{3,4} SFG experiments involved ~ 100 nm layers, about 100 molecular diameters thick.^{1,12,16,17,19–21}

Using such thin samples has the dual disadvantages of requiring monolayer fabrication techniques and low spectroscopic sensitivity. Self-assembled monolayers^{2,8} provide a simple solution to the fabrication issues. SFG spectroscopy⁵ with resonant IR pulses⁶ is sensitive enough and selective enough to probe a layer that is effectively ~ 1.5 Å thick, providing atomic scale depth resolution of the surface of a molecular material.^{3,4} The sensitivity results from the technique being a resonant coherent process.¹ The selectivity results from the SFG probe being symmetry forbidden in isotropic media. With alkane SAMs in the usual all-trans configuration,² only the terminal methyl groups are SFG-active,²² because the methylene units are locally centrosymmetric.

Using such a thin sample layer, where the shock front transit time is reduced to < 50 fs, effectively eliminates shock propagation as a factor in the time resolution. Other factors come to play, and in our experiments the time resolution becomes limited primarily by the vibrational dephasing time constant for the terminal methyl groups.⁴

A long-standing problem in condensed phase reaction dynamics appears in the comparison of experiment to atomistic simulations. Ultrafast spectroscopy measurements are usually the most germane, because they can match the relevant time and length scales. However, in classical mechanics there is a fundamental problem with photoexcitation, which must be handled in an ad hoc manner. Shock compression can be directly simulated with a moving boundary or a simulated impact plate,²³ but huge computer power is needed because the shock front advances through the sample at ~ 50 atoms/ps. With advancing computer power, atomistic simulations of shock compression have recently flourished.²⁴ These simulations provide information about the structure of the shock front with atomic scale resolution, and so it is a significant goal to develop experimental techniques to probe a shock front with similar resolution.

In previous papers, we briefly discussed the experimental technique³ and presented a preliminary comparison⁴ of ODT/Au and PDT/Au. Here we present a detailed description of monolayer shock compression that includes comparisons of flexible long-chain molecules with more rigid short-chain molecules and effects of Au vs Ag substrates. Because shock compression raises both monolayer pressure and temperature, we also present an extensive series of isobaric heating data.

2. Background

A. Self-Assembled Monolayer Structure. ODT and PDT form highly ordered all-trans SAMs on both Au and Ag. On Au, the chains form a $(\sqrt{3} \times \sqrt{3})R30^\circ$ lattice⁹ with the chains tilted $\sim 30^\circ$ from normal. Besides the overall chain length, the most significant difference between ODT/Au and PDT/Au is the methyl tilt angle. Keep in mind the distinction between chain tilt and methyl or phenyl tilt, which are generally different. Due to the zigzag all-trans alkane chain structure, in the even chain ODT the methyl tilt is $\sim 23^\circ$ and in the odd chain PDT it is $\sim 60^\circ$.

The packing of ODT on Ag is denser and the chains are more upright than on Au. Instead of the $(\sqrt{3} \times \sqrt{3})R30^\circ$ lattice with

21.6 Å²/chain,⁹ ODT/Ag forms on a $(\sqrt{7} \times \sqrt{7})R19.1^\circ$ lattice, with 16.9 Å²/chain²⁵ with a chain tilt⁹ of $\sim 10^\circ$ and a methyl tilt of $\sim 33^\circ$.

The short-chain aromatic thiol BMT has not been studied much. The primary degrees of freedom are the conformation of the S–C–phenyl bond that largely determines the phenyl tilt, and the phenyl twist. A simulation of the BMT/Au structure²⁶ gives a hexagonal lattice in the anti configuration with the ring upright above the Au plane, as opposed to the gauche configuration with the ring lying on the Au surface. The phenyl groups are arranged with the usual²⁷ herringbone packing.

B. Sum-Frequency Spectroscopy. Vibrational SFG is a second-order nonlinear process with a mid-IR pulse tuned near a vibrational resonance^{5,6,22} and a nonresonant visible pulse. The SFG intensity depends on the second-order susceptibility, $\chi^{(2)}$,

$$I_{\text{sum}} \propto |\chi^{(2)}|^2 I_{\text{vis}} I_{\text{IR}} \quad (1)$$

which is a third-rank tensor that depends on the orientational average of the molecular hyperpolarizability of the surface molecules and the surface coverage or concentration. In the dipole approximation all elements of $\chi^{(2)}$ vanish in centrosymmetric media, but not at surfaces or interfaces.

For molecules adsorbed at a metal surface, $\chi^{(2)}$ has a resonant contribution from molecular vibrational transitions and a broad nonresonant contribution from the metal surface.²² The SFG intensity in this case is proportional to

$$I_{\text{sum}} \propto |\chi_{\text{R}}^{(2)} + \chi_{\text{NR}}^{(2)}|^2 = |\chi_{\text{R}}|^2 + |\chi_{\text{NR}}|^2 + 2|\chi_{\text{R}}||\chi_{\text{NR}}| \cos \delta \quad (2)$$

where both contributions to $\chi^{(2)}$ are complex, and δ is the phase difference. The phase of the nonresonant term is constant across a broad frequency range whereas the phase of a resonant transition varies across the transition. For alkanes adsorbed on Au and Ag, on resonance the phase difference $\delta \approx \pi$. In our experiments $|\chi_{\text{NR}}| > |\chi_{\text{R}}|$, so the resonant contribution arises primarily from the cross-term in eq 2. Under these conditions, the molecular vibrational resonances are effectively heterodyne-detected against a local oscillator provided by the metal surface, and the resonances appear as dips in the nonresonant signal.^{28,29} The depth of a vibrational resonance in this case has an approximately *linear* (rather than quadratic) dependence on the molecular hyperpolarizability and surface coverage.

For all-trans alkyl chains the methylene backbone is locally centrosymmetric, so only the terminal methyl group contributes to the SFG signal.²² The SAMs are bound to a polycrystalline surface and in addition are thought to form 50–70 Å domains,³⁰ so an SFG spectrum is an average over a broad range of azimuthal angles ϕ with a narrower range of polar angles θ . With azimuthal and mirror symmetry, only 4 elements of $\chi^{(2)}$ are independent.²² On a dielectric surface, polarization-dependent SFG can unambiguously determine molecular orientation.³¹ However, on a conducting surface, the field vanishes in the plane of the conductor, and only the *zzz* element of the susceptibility tensor contributes significantly to the SFG signal.²⁸ This element is sensitive to the polar angle θ . Without knowing the molecular transition intensity accurately, it is difficult to determine θ from SFG spectra. However, in dynamic reorientation studies where the time-dependent SFG signal can be compared to its value in the known equilibrium structure, it is possible to determine the instantaneous value of θ .

The orientation of a terminal methyl group can be described by the three Euler angles, θ , ϕ , and ψ , where θ is the methyl tilt angle, that is, the angle of the methyl C_{3v} (molecular z')

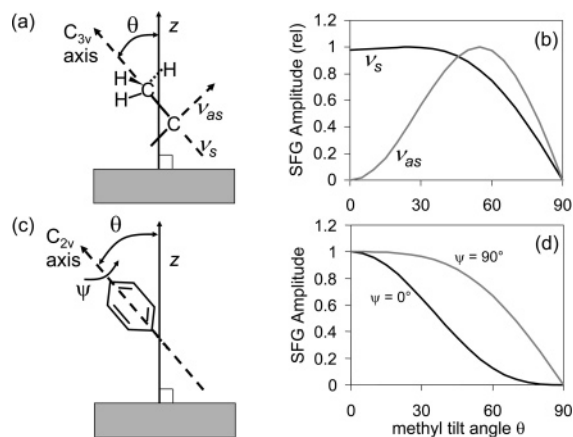


Figure 1. (a) Tilt of the alkane SAM terminal methyl C_{3v} axis described by tilt angle θ . (b) Tilt angle dependence of SFG intensity for the methyl symmetric ν_s and asymmetric ν_{as} stretch modes. (c) The orientation of a phenyl ring in BMT is described by tilt angle θ and twist angle ψ . (d) Tilt angle dependence of SFG intensity for phenyl C–H stretching with the ring lying on its edge ($\psi = 90^\circ$) or on its back ($\psi = 0^\circ$).

axis relative to the surface normal (z axis), shown in Figure 1a. ϕ is the azimuthal angle and ψ is the angle of the rotation about the methyl C_{3v} axis. To relate these angles to the SFG intensity, it is necessary to transform the molecular hyperpolarizability from internal molecular coordinates to the laboratory frame.^{32,33} To calculate the dependence on the tilt angle θ for the nominally³⁴ doubly degenerate ν_{as} transition, it is necessary to assume free rotation of the methyl group (average over all angles ψ). For the singly degenerate ν_s transition this additional assumption is not needed.

For the ν_s transition, the resonant SFG amplitude is given by

$$A_{zzz,s} = N_s \beta_{zz'z'} [r \langle \cos \theta \rangle + (1 - r) \langle \cos^3 \theta \rangle] \quad (3)$$

where β is the hyperpolarizability, r is the depolarization ratio

$$r = \frac{\beta_{xx'z'}}{\beta_{zz'z'}} \quad (4)$$

and the primes denote the molecular coordinates. For ν_{as} ,

$$A_{zzz,as} = \beta_{zz'x'} (\langle \cos \theta \rangle - \langle \cos^3 \theta \rangle) \quad (5)$$

where the brackets denote orientational average. The computed angular dependence of the relative SFG intensities of methyl C–H stretching transitions is shown in Figure 1b. For $\theta = 0$ (upright methyl), the ν_s intensity is maximum and the ν_{as} intensity vanishes. For $\theta = 90^\circ$ (C_{3v} axis bent parallel to the surface), both transitions vanish. However, keep in mind that the ν_{as} calculation may be less reliable,³⁵ because methyl is quite likely not a free rotor, especially under compression.

For BMT we see CH stretching signals from the phenyl group but we so far have seen nothing from the methylene moiety. The substituted aromatic ring exhibits C_{2v} symmetry. As shown in Figure 1c, θ is the tilt angle of the C_{2v} axis relative to the surface normal and ψ describes the twist of the phenyl group about this axis. The ring lies in the molecular $x'z'$ plane (z' is equivalent to the C_{2v} axis). With $\psi = 0^\circ$ the ring faces the surface; with $\psi = 90^\circ$ the phenyl ring is on edge relative to the surface. The nonlinear susceptibility is given by

$$A_{zzz} = N_s \beta_{zz'z'} [(1 - \gamma \langle \sin^2 \psi \rangle) \langle \cos^3 \theta \rangle + \gamma \langle \sin^2 \psi \rangle \langle \cos \theta \rangle] \quad (6)$$

where

$$\gamma = \frac{\beta_{xx'z'}}{\beta_{zz'z'}} \quad (7)$$

The computed angular dependence of the SFG signal is shown in Figure 1d. As with the alkanes, the signal vanishes only with large tilt angle (phenyl tilted down to the plane) regardless of phenyl twist angle.

C. SAMs under Static or Slowly Varying Loads. The mechanical properties of SAMs have been studied by mechanical and optomechanical techniques. The mechanical methods include atomic force microscopy (AFM)^{36–38} and frictional force microscopy (FFM).^{39,40} Alkanethiol SAMs with even numbers of carbon atoms were compressed to static pressures of <1 GPa with an AFM tip. At a critical load of ~ 0.2 GPa, the SAM surface becomes disrupted.⁴¹ Simulations suggested that this disruption occurs by the formation of gauche defects near the methyl terminus of the chains.⁴² A gauche defect helps relieve uniaxial stress by making the alkane chains shorter and wider. Collective tilting of the monolayer molecules under compression has also been observed.⁴⁰ With even greater strains, an AFM tip was actually able to scratch the metal surface, indicating that SAM molecules were uprooted and driven out of the compressed region.⁴¹

FFM studies have found an interesting chain alternation effect. Alkanes with odd numbers of carbon atoms evidence slightly higher friction than even chains in the small-load limit.³⁹ This difference was attributed to the greater methyl tilt of the odd chains which changes the interaction between the terminal methyl group and the probe. A recent comparison of shorter (C4) and longer (C12) even-carbon chains on Au and Ag reveals significantly lower friction on Ag, which was explained as the higher chain density on Ag hindering the formation of gauche defects and other chain deformations.

SFG has been used as a probe of even-carbon alkane SAMs under static pressure produced by a transparent anvil. The resonant SFG intensity of the terminal methyl groups decrease as the SAM is compressed above^{44–48} 10 MPa. The SFG signal returned elastically when the pressure was released. SFG signal drop was discussed only in broad general terms that attributed the loss of signal to reorientation or disordering of the methyl terminus or flattening of the molecular axis.

D. SAMs at Elevated Temperatures. Spectroscopic investigations of heated alkanethiol monolayers in inert atmosphere or vacuum suggests reorientation of the alkyl chains.⁴⁹ Simulations^{50,51} indicate that the chain tilt decreases with increasing temperature, accompanied by an increase in disorder and greater reorientational freedom. Alkanethiol monolayers have been observed to desorb at temperatures of 175–225 °C.^{52,53}

E. Laser Driven Shock Waves. Laser-driven shock waves are generated with the arrangement shown in Figure 2a. The shock front passes over the SAM and continues on into a nearly impedance-matched layer of contact fluid used to maintain a continual load on the SAM and delay shock reverberations from the CaF_2 window. A femtosecond near-IR pulse $\sim 125 \mu\text{m}$ in diameter passes through a glass substrate and is absorbed at the glass-metal interface. An expanding confined plasma is generated,^{54,55} which drives a shock wave through the metal layer into the sample. The compression process should be viewed as planar.^{18,56} Although the shock does have a radial pressure profile due to the near-Gaussian laser intensity profile, the optics are arranged so the SFG signal is generated from the uniform region at the center of the beam. In addition the pulse

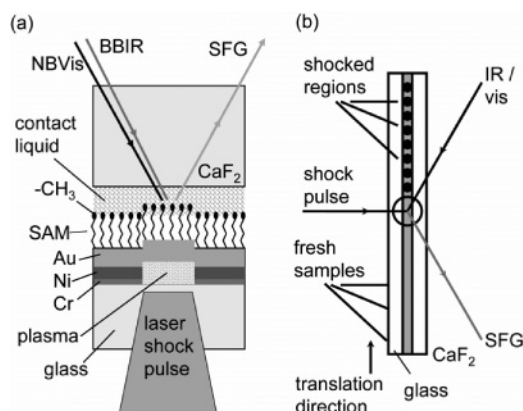


Figure 2. (a) Schematic of a single element of a shock target array. A laser drive pulse generates a 5–10 GPa shock in Ni that propagates through an impedance-matched Au layer before reaching the SAM. The contact liquid is perdeuterated ethylene glycol. Vibrational sum-frequency generation (SFG) spectroscopy monitors CH stretch transitions of the terminal methyl groups. (b) The shock target array is translated through the intersection of the shock generation pulse and the SFG probe pulses. Each laser shot hits a fresh sample.

profile actually flattens out as it propagates through the glass due to nonlinear optical interactions. This flattening increases the diameter and uniformity of the central region of the shock front.¹⁸

We use a trilayer metallic thin film,³ consisting of 25 nm Cr, 100 nm Ni and 75 nm Au or 100 nm of Ag. The small-amplitude shock velocity⁵⁷ in these metals is 5.2 km/s for Cr, 4.6 km/s for Ni, 3 km/s for Au, and 2.8 km/s for Ag. The Cr is used as an adhesion promoter and plasma generation medium. The Ni is needed as an insulation layer. Femtosecond laser pulses directly on Au create hot ballistic electrons that run through the Au much faster⁵⁸ than the shock front,⁵⁹ which would lead to undesirable electron preheating of the SAM and transient reflectivity changes in the metal surface⁵⁹ prior to shock front arrival. The electron mean-free path⁵⁸ in Ni is much smaller than the thickness of our Ni layers.

F. Estimated Pressure in SAMs. A shock is generated in Ni, which then passes through an Au or Ag layer and then through the SAM and contact liquid. We begin by estimating the pressure in the Ni layer and then determine how the pressure changes in subsequent layers.

Femtosecond laser generated shocks in Ni thin films have been previously characterized by free-surface interferometry. The shock front has a steep 2–4 ps rise to a peak pressure⁵⁴ of 5–10 GPa, followed by a gradual decline to ambient pressure over tens of picoseconds.^{18,54,60,61} With a fluence of ~ 4.5 J/cm² and a Ni layer 250 nm thick the shock pressure was 16 GPa, and with a 467 nm thick Ni layer the pressure was⁵⁴ 10 GPa. Our laser fluence (beam center) is 2 J/cm² and the total thickness of Ni plus Au plus Cr is ~ 200 nm. In this fluence regime, the shock pressure is roughly a linear function of fluence,⁶¹ so our estimated shock pressure in Ni is 7 GPa. In view of uncertainties in comparing the temporal and spatial envelopes from different femtosecond lasers, we conservatively cite a broad error range of pressure, $P = 5$ –10 GPa.

When a shock with incident pressure P_i propagates between layers with impedances Z_a and Z_b , the reflected pressure P_r depend on the shock impedance $Z = \rho c$, where ρ is the density and c the acoustic velocity, through the relation⁶²

$$P_r = \frac{P_i[(Z_a/Z_b) - 1]}{(Z_a/Z_b) + 1} \quad (8)$$

TABLE 1: Shock Wave Parameters^a

	m	b (km/s)	ρ_0 (g/cm ³)	c_0 (km/s)
Ni	1.44	4.59	8.88	5.79
Au	1.54	3.07	19.24	3.25
Ag	1.59	3.24	10.50	3.65
polyethylene (PE)	2.57	2.34	0.95	2.36

^a The Hugoniot is expressed as $U_s = mU_m + b$. Data for Ni, Au, and Ag from ref 57, data for PE from ref 63.

The shock properties of materials are usually characterized by the shock Hugoniot, which is usually written in the form

$$U_s = mU_m + b \quad (9)$$

where U_s is the shock velocity, U_m is the material velocity and m and b are material constants⁵⁷ listed in Table 1. The volume compression factor $\Delta V = (V_i - V_f)/V_i$ is

$$U_s = \frac{b}{1 - m\Delta V} \quad (10)$$

and the pressure P is

$$P = \frac{b^2\Delta V}{V_0(m\Delta V - 1)^2} \quad (11)$$

Using the parameters in Table 1, there is an excellent impedance match between Ni and Au, with Ag having lower impedance. For the Ni/Au interface eq 8 gives $P_r/P_i = 0.098$, so the transmitted pressure is $>90\%$ of the incident pressure. Au has about twice the density and one-half the acoustic velocity as Ni,⁵⁷ so as a shock propagates from Ni to Au, the velocity drops from ~ 4.6 km/s to ~ 3 km/s with little loss of pressure. For the Ni/Ag interface, eq 8 gives $P_r/P_i = 0.3$, so the transmitted pressure is $\sim 70\%$ of the incident pressure.

We do not have a detailed knowledge of the shock parameters for the SAMs, although clearly the SAM layers have much lower shock impedances than Au or Ag. It is natural to look to other hydrocarbons for reasonable estimates of SAM pressures. A reasonable model system with the proper compression behavior should, we believe, approximately match the density of the SAM. In ODT/Au, the area per chain is 21.7 Å² and the effective SAM height is ~ 20 Å. This gives a volume per chain of 434 Å³. The molar mass of ODT is 285.56 g/mol, which gives an effective density of $\rho = 1.1$ g/cm³. However, there are edge effects due to the sulfide anchor and the terminal methyl, so we feel a better figure-of-merit is the density of $-\text{CH}_2-$ methylene groups, which for ODT/Au is $\rho_{\text{CH}_2} = 4 \times 10^{22}$ cm⁻³. Beattie et al.⁴⁶ have suggested liquid hexadecane as a model for SAM compression. However, the density of hexadecane ($\rho = 0.77$ g/cm³, $\rho_{\text{CH}_2} = 3 \times 10^{22}$ cm⁻³) is quite a bit too low. Amorphous polyethylene (PE), where $\rho_{\text{CH}_2} = 4 \times 10^{22}$ cm⁻³, having extensively tabulated shock data,⁶³ is our choice for a model for SAM compression.

The SAM impedance is quite a bit smaller than either Au or Ag. In this case the SAM is poorly coupled to the substrate and P becomes quite sensitive to the SAM impedance, so we will use different method to estimate P . Owing to the much higher shock impedance of the metal substrate, we can approximate the shock in Au or Ag as emerging at a free surface. This estimate only slightly overestimates the shock pressure in the low-impedance SAM.²¹ The shock pressure in the SAM is the pressure expected for a shock driven at the free-surface velocity of the Au or Ag. The free-surface velocity²¹ is just twice U_m . For instance, for a 10 GPa shock in Au, $U_m = 0.24$

km/s and the free-surface velocity is 0.48 km/s. Then for a shock in PE where $U_m = 0.48$ km/s, $P = 1.6$ GPa. Thus our best estimates for the shock pressure for SAMs on Au is $P = 1.0$ – 1.6 GPa. With Ag there is a worse impedance mismatch at the Ni/Ag interface but a better match at the Ag/SAM interface, leading to a similar estimated pressure for ODT/Ag of $P = 0.9$ – 1.4 GPa.

Shocks in this pressure range in PE would have $U_s \sim 3.5$ km/s, $U_m \sim 0.5$ km/s and $\Delta V = 0.1$ – 0.13 . Keep in mind that this value of ΔV describes compression of the methylene ($-\text{CH}_2-$)_n backbones of the SAMs. It seems likely that the terminal methyl groups are more compressible than this backbone, so these values of ΔV could be a bit of an underestimate. A compression of 0.1 in ~ 3 ps corresponds to a strain rate of $3.3 \times 10^{10} \text{ s}^{-1}$.

G. Shock Temperature. Shock compression is a cycle of irreversible compressive heating and nearly reversible expansive cooling. For a material initially at temperature and volume (T_i , V_i), the shock temperature increase is

$$T_f = T_i \exp(\Gamma \Delta V) + \Delta T_{\text{irr}} \quad (12)$$

where Γ is the Grüneisen coefficient.⁶⁴ The first term is the temperature increase in a reversible (isentropic) compression, and the second term is the additional temperature rise due to the entropy increase across the shock front. The value of ΔT_{irr} depends explicitly on the path; an expression for a fast single-stage compression is given in ref 16. For weak shocks, the first term is dominant. The shock temperature cycle on time scales ($< 100 \mu\text{s}$) when thermal conduction can be neglected can be represented as $T_i \rightarrow T_f$ in the compression stage and $T_f \rightarrow T_i + \Delta T_{\text{irr}}$ in the expansion stage.

Equation 12 shows that the temperature rise is greater for more compressible materials with larger Γ . Larger Γ is associated with materials having more anharmonic intermolecular or interatomic force fields.²⁷ The SAM is a thin layer in contact with a practically incompressible metal substrate that is heated very little and a deuterated ethylene glycol contact liquid that heats more. We can estimate shock temperatures for the metal substrates and for the contact liquid, using glycerol data^{57,65,66} as a substitute for glycol. Estimating the SAM parameters is much more uncertain. However, except for a brief period of ~ 10 ps needed to reach thermal equilibrium, the SAM temperature will be determined by its surroundings. The SAM anchor will equilibrate with the metal substrate and the SAM terminal group will equilibrate with the contact liquid.

For Au with 7 GPa shocks the relative volume change $\Delta V = 0.04$,⁵⁷ and $\Gamma \approx 2$,⁶⁴ so the peak temperature jump from eq 12 will be ~ 25 K. Assuming a planar single-stage compression, $\Delta T_{\text{irr}} < 5$ K.¹⁶ For glycerol⁵⁷ at 1.6 GPa, $\Delta V = 0.13$ and $\Gamma = 1.2$,⁶⁵ the peak temperature jump is ~ 50 K and $\Delta T_{\text{irr}} \approx 5$ K. Thus the SAM anchor at the Au substrate heats only slightly, whereas the SAM terminal methyl or phenyl group in contact with the glycol layer undergoes larger temperature swings, $25^\circ\text{C} \rightarrow 75^\circ\text{C}$ during the compression stage, and $75^\circ\text{C} \rightarrow 30^\circ\text{C}$ during the unloading stage.

H. Uniaxial Compression, Shear, and Shock Unloading. The nature of shock loading and unloading depends a great deal on the specific sample geometry illustrated in Figure 3. Figure 3 is not drawn to scale. The diameter of the shocked region, which is about equal to the laser beam diameter, is more than 10^2 times the shock run distance $< 1 \mu\text{m}$. The laser-driven shock geometry is designed to mimic the more conventional process of planar shock generation by a flat impact plate.¹¹ In Figure 3,

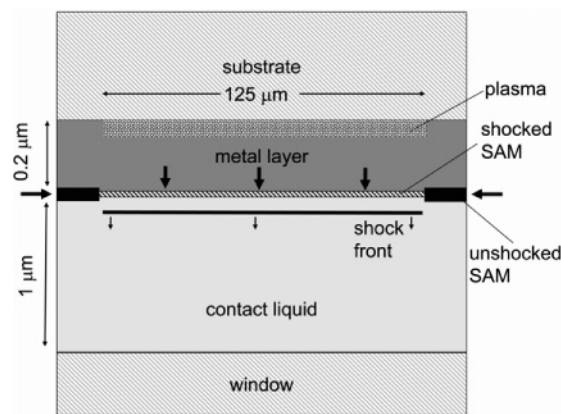


Figure 3. Geometry for shock loading and unloading (not to scale). The diameter of the shocked region is 10^2 times greater than the shock run distance. The SAM layer is inertially confined in the radial direction, as if the SAM were compressed by a piston (the metal layer) in a cylinder with rigid walls. The stress on the SAM layer (heavy arrows) results from a longitudinal compressive stress from the metal layer plus a transverse shear stress from the cylinder walls. When the plasma stops expanding, the metal layer retreats back toward the substrate, launching a rarefaction wave that relieves the load on the SAM.

the metal layer represents the impact plate; it is $\sim 0.2 \mu\text{m}$ thick and $\sim 125 \mu\text{m}$ in diameter.

When the shock front passes over the SAM, the SAM should be viewed as a thin disk confined in a rigid cylinder compressed by a flat piston.⁶⁴ The rigid cylinder analogy is used because the SAM is inertially confined in the transverse (radial) direction because of its large diameter. Thus the net force on the SAM can be viewed as resulting from the longitudinal stress (the compressive load) from the piston and an inward transverse stress (the shear load) from the cylinder walls.⁶⁴

Shock unloading begins when the plasma cools and its expansion stops. At this point the plasma-metal interface begins to retreat toward the glass substrate (see Figure 3), launching a rarefaction wave. The rarefaction wave from the window runs up to the SAM, and relieves the compressive load. Rarefaction waves are also generated along the circumference, but to have an effect, these must travel a much greater distance inward along the cylinder radius. Unlike a shock front which steepens as it runs,⁶⁴ rarefaction waves disperse as they run, so unloading is slower and more reversible than compression.⁶⁴ The duration of the unloading process depends on the impactor thickness and its acoustic dispersion, but it will be on the order of the ~ 25 ps transit time of the rarefaction wave through the metal layer. The pressure falloff can be fit to an exponential function with a fall time of tens of picoseconds.^{18,54,60,61} The shock compression temporal envelope can be fit with a phenomenological function of the form

$$f(t) = (1 + \exp[-(t - t_0)/t_r] + \exp[(t - t_0)/t_f])^{-1} \quad (13)$$

where the constants $t_r = 1.1$ ps and $t_f = 9.6$ ps are obtained by fitting the highly elastic shock response data in Figure 5b having rise and fall times (10% to 90%) of 4 and 25 ps, respectively, and t_0 indicates the arrival time of the shock front at the SAM. To compare eq 13 to the vibrational response function, which drops from 1 to 0, in Figures 5–8 we have plotted the function $1 - f(t)/f_{\text{max}}(t)$, where $f_{\text{max}}(t)$ is the maximum value of $f(t)$.

I. Elastic and Viscoelastic Compression. A viscoelastic material exhibits a damped response to shear. In acoustic damping,⁶⁷ attenuation increases with amplitude and frequency, which is interpreted as resulting from a frequency- and

amplitude-dependent viscosity. Viscoelasticity is also commonly used to describe material response to uniaxial planar shock compression,^{11,62} where the strain rates can exceed those in acoustic experiments by 10^5 or more.

In the hard-wall cylinder analogy where uniaxial compression creates both compressive and shear stress, there is a critical compressive stress P_{cr} that defines the elastic limit. At P_{cr} , the off-diagonal elements of the stress tensor $\sigma_{x'y'}$ reach a critical shear stress σ_{cr} where the sample undergoes mechanical failure and undergoes a shape change to equalize the load in all directions. This reduces the compressive stress and increase the transverse stress to produce a more hydrostatic load.⁶⁴ If a hydrostatic condition is reached during the shock, the diagonal elements of the stress tensor become equal and the off-diagonal elements vanish.

In viscoelastic shock compression the shock front consists of two parts, a faster elastic part and a slower plastic deformation part.⁶⁸ As the front propagates, the elastic part moves ahead and disperses whereas the plastic part lags behind and remains steep. The rise time of the steeper part is explained by a phenomenological shock viscosity.⁶⁹ In analogy to ordinary viscosity, the shock viscosity is a measure of the rate of mechanical deformation or shape change at high strain rates.

In classic shock literature, shape change in metals is described as resulting from plastic deformation.¹¹ Shape change in brittle materials such as Si is described as wholesale lattice destruction to produce a fluid powder.¹¹ In a SAM, which is a forest of molecular chains, we have the interesting possibility of interpreting the shape change in terms of specific molecular deformations^{12,13} that result in shorter but fatter chains. Elastic deformations that can cause a SAM to become shorter and fatter involve tilting the terminal methyl group toward the surface plane and increasing the whole-chain tilt angle. Deformations beyond the elastic limit are those that involve surmounting conformational energy barriers.^{12,13} The simplest model for chain shortening is *trans*-to-*gauche* isomerization; various types of entanglements among multiple chains may also be possible. Whole chains may be displaced from their anchor sites and driven to new sites outside the shocked region,⁴¹ but this is clearly impossible on the subnanosecond time scale for a 125 μm diameter shock.

3. Experimental Section

A. Sample Fabrication. The shock target arrays³ depicted in Figure 2 were fabricated on $50 \times 50 \times 1.6 \text{ mm}^3$ borosilicate glass substrates (Chemglass, Inc.). Evaporated metal films were deposited on eight substrates at a time. The film thicknesses were measured during deposition with a quartz microbalance. The total thickness could be checked afterward by surface profilometry. Our evaporator had fixtures for only two metal sources, so Cr and Ni were deposited and then the vacuum was broken to load Au or Ag for the third deposition. The nominal layer thicknesses were 25 nm Cr, 100 nm Ni, and 75 nm Au or Ag, for an overall thickness of $\sim 200 \text{ nm}$. All displayed data sets refer to experiments performed on the eight nearly identical thickness samples produced in a single batch. There was a thickness variation from batch to batch of $\pm 10 \text{ nm}$, so the shock front arrival at the SAM could vary by a few picoseconds between batches.

To measure the shock propagation delay and shock velocity through Au, we produced several sets of samples that were identical except for the Au layer thickness. To produce such a set, eight substrates were coated with Cr and Ni. Half of these along with some bare reference substrates were then coated with

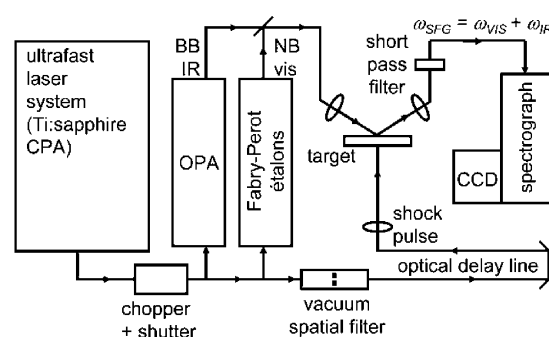


Figure 4. Schematic of the optical setup used for the laser shock experiments. CPA = chirped-pulse amplifier; OPA = optical parametric amplifier; CCD = charge-coupled array detector; BBIR = broad band mid-IR pulse; NBvis = narrow-band visible pulse.

Au. The other half plus other reference substrates were coated with a larger amount of Au. This resulted in a set of substrates with essentially identical Cr and Ni layers, four having thinner and four having thicker Au layers. Profilometry on the reference substrates was then performed to determine the Au layer thicknesses.

The SAMs were produced by immersing the substrates in 1 mM solutions in deoxygenated ethanol for 3 h, followed by storage under neat ethanol. ODT, a solid, was recrystallized from ethanol. PDT and BMT, both liquids, were used as purchased without further purification.

Immediately prior to spectroscopic measurements, a substrate was removed from the ethanol storage bath, rinsed with steam-distilled water, and blown dry. Two drops of the contact fluid, perdeuterated ethylene glycol were placed in the center of the sample. A 2 in. diameter CaF_2 window was placed over the fluid, spreading the fluid to a capillary thin film estimated at 1–2 μm thick. The fluid and window are transparent in the C–H stretching region and they provide inertial confinement for the SAM.

B. Laser System. Figure 4 shows a schematic of the shock/SFG laser system.³ Ti:sapphire femtosecond pulses were input from an oscillator to a 1 kHz chirped pulse amplifier, which included a regenerative amplifier stage and a two-pass power amplifier.⁷⁰ The compressed 3.7 mJ output pulses at 804 nm had a pulse duration⁴ $< 170 \text{ fs}$. An optical chopper reduced the repetition rate to 100 Hz. An electronic shutter could be used for single-shot operation. The laser output was split into a shock generation leg and a probe leg. The shock generation pulse (115 μJ , $1/e^2$ diameter 125 μm , 170 fs, 100 cm^{-1} fwhm) entered a vacuum spatial filter with a diamond pinhole to improve the beam profile, a variable delay line, and a lens to focus the pulse onto the target array.

The probe leg was further split into two parts for broadband multiplex SFG spectroscopy²⁹ with *ppp* polarization. One part pumped an optical parametric amplifier (OPA, Light Conversion TOPAS 4/800 DFG) to generate 2950 cm^{-1} broad-band mid-infrared pulses (BBIR; 30 μJ , $1/e^2$ diameter 250 μm , $\sim 200 \text{ fs}$ duration, 250 cm^{-1} fwhm), and the other was filtered through a pair of Fabry–Perot etalons (TecOptics, Inc.) to produce an 804 nm narrow-band visible pulse (NBvis; 1.5 μJ , $1/e^2$ diameter 100 μm , $\sim 4 \text{ ps}$ duration, fwhm 5 cm^{-1}). The BBIR and NBvis pulses were made collinear with a dichroic mirror (Altechna Ltd.) and cotemporal with a variable delay line on the NBvis beam. The $\sim 650 \text{ nm}$ sum-frequency signal was detected with a 0.25 m spectrograph and CCD.

C. Shock Compression Spectra. The assembled sample and window were mounted on an *xy* translation stage. Because the

NBvis pulse has an ~ 4 ps duration, time zero is defined by the temporal intersection of the femtosecond shock and femtosecond BBIR pulses at the sample plane. Time zero was determined using a 1 mm thick polycrystalline ZnS (Cleartran) window at the sample location, which generates an easily seen SFG signal.

The NBvis beam diameter is smaller than the BBIR, so the critical alignment step is to make the NBvis beam slightly smaller in diameter and centered on the region that is uniformly shocked. We would fire a single shock pulse and observe the reflected NBvis beam. The shock pulse causes the metal film to disintegrate, leaving behind a nonreflecting spot that denotes the shocked region. When the alignment is correct, the reflected visible beam vanishes completely after a shock. This critical alignment was rechecked prior to acquiring each shock SFG spectrum. After alignment, a reference spectrum was obtained by accumulating thousands of pulses with no shock. Then with the shock pulses at 100 Hz, the sample stage was translated so that each shot hit a fresh region of the sample as the SFG signal was acquired.

D. Variable Temperature Studies. We characterized the thermal properties of the SAMs with glycol contact fluid by placing the sample assembly in an oven. The oven had four thermocouples at different locations which allowed us to trim the insulation and heating tape to guard against temperature gradients. The heating rate was not under precision control, but the temperature rise from ambient to 120 °C occurred over a few hours, so the average heating rate was on the order of 10^{-2} K/s. SFG spectra acquisitions were typically 20–30 s at 1 kHz. Care was taken to avoid laser damage of the probed area, which became more likely at elevated temperatures. If damage occurred, as assessed by a sudden drop in the SFG signal intensity, the sample was translated to a fresh spot.

E. Data Analysis. As explained in section 2B, the depth of the resonant CH stretching signal against the nonresonant background is an approximately linear rather than quadratic function of the molecular hyperpolarizability. The depths of the resonant features in the unshocked spectrum, I_{ns} , and in the shocked spectrum at delay time t , $I_{\text{s}}(t)$, were measured and each normalized to the overall height of the nonresonant SFG signal, I_{nr} . The time dependent data are then presented as normalized vibrational response functions of the form

$$I(t) = [I_{\text{s}}(t)/I_{\text{nr}}]/[I_{\text{ns}}/I_{\text{nr}}] \quad (14)$$

Due to the nature of these experiments, it was not possible to compute error bars for each data point. A single batch of samples was enough to obtain only one time series of data. Comparisons among different sample batches were hindered by variations in thickness and time zero. For each type of monolayer data were obtained several times. Qualitative features of the data discussed here were those that were observed consistently on each data run. Judging from the scatter in adjacent data points, the estimated error bound for each data point is 10–15%.

4. Results

A. Static SFG Spectra. SFG spectra for PDT/Au, ODT/Au, ODT/Ag, and BMT/Au are shown at the bottom of Figures 5a, 6a, 7a, and 8a, respectively. The signal extending over SFG wavenumbers 2500–3300 cm^{-1} mirrors the BBIR pulse envelope.²⁹ The shape of this envelope is sensitive to OPA alignment and varies somewhat from day to day. The CH stretching resonances of the SAMs are the sharper 10–15 cm^{-1} wide dips^{28,29} in the spectrum. In the alkanethiol SAMs, a single ν_{as} transition is observed, whereas ν_{s} is split in two by Fermi

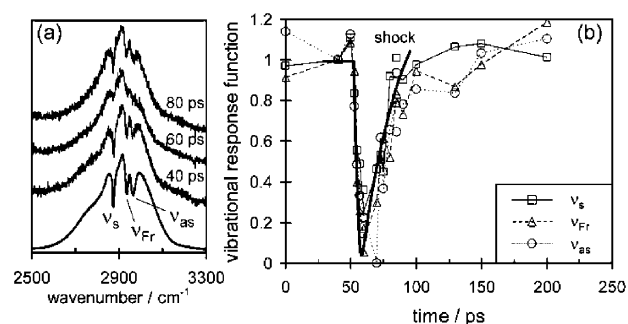


Figure 5. (a) SFG spectra of PDT/Au with shock compression. The bottom spectrum is obtained without shock, with extensive integration time. The shock front arrives at the monolayer surface ~ 60 ps after time zero denoting the arrival of the shock-generation laser pulse. (b) Time-dependent SFG intensities of three PDT transitions, plotted as normalized vibrational response functions (eq 14). The curve labeled “shock” is the putative time-dependent envelope of shock compression, fit to eq 13. SFG signal loss and recovery closely track the shock envelope, indicating that PDT/Au shock compression is largely elastic.

resonance. One of the split resonances ν_{s} has mainly symmetric stretch character and the other ν_{Fr} mainly bend overtone character. The greater tilt angle in PDT/Au versus ODT/Au results in proportionately more ν_{as} intensity in PDT/Au.⁷¹ In BMT only one CH stretching transition is observed, which has been assigned as the ν_2 transition of the phenyl group.⁷¹

B. Shocked PDT/Au. Figure 5a shows a series of SFG spectra of PDT/Au taken at different shock-probe delay times. Only a few representative spectra from the data set are shown, offset for clarity. In shock spectra, there can be a small and variable contribution from the visible continuum emission of the shock drive plasma that can be seen by the detector after the metal layer becomes fragmented. This plasma emission is why the nonresonant signal seems to broaden or develop sidebands in the shock spectra.

The resonant CH stretch transitions do not broaden or shift when the shock arrives. They simply lose intensity and then regain intensity after the shock unloads. The time dependence of the vibrational response functions for PDT/Au is shown in Figure 5b. The resonant SFG signals drop precipitously near $t = 60$ ps, nearly vanishing. Following this decrease, the SFG signal recovers almost entirely. The curves in Figures 5–8 labeled “shock” represent the putative temporal envelope of shock compression as explained in sections 5B and 5C. The ν_{s} signal appears to accurately track the shock envelope. However, the ν_{as} signal recovers instantaneously to only ~ 0.8 of its initial value. There then appears to be a slower component in the signal recovery with an amplitude of 0.1–0.2. The present quality of our data prevents a detailed analysis of this slower component, but because it is observed over an ~ 60 ps time interval, we will term it an ~ 30 ps process without expressing an opinion regarding its functional form. The nearly complete and immediate recovery of the PDT/Au vibrational response functions indicate that shock compression should be characterized as elastic.

C. Shocked ODT/Au. Figure 6 shows shock data for ODT/Au. As with PDT, the SFG signals lose intensity abruptly in < 4 ps when the shock front arrives, and the resonant SFG transitions neither shift nor broaden. The SFG signal recovery for ODT/Au exhibits marked differences from PDT/Au. (1) The post-shock vibrational response functions do not return to their original levels, even at the longest times (~ 1 ns) that data can be acquired. (2) An ~ 30 ps transient is again observed, but now it can be seen in all three resonant transitions, and it is

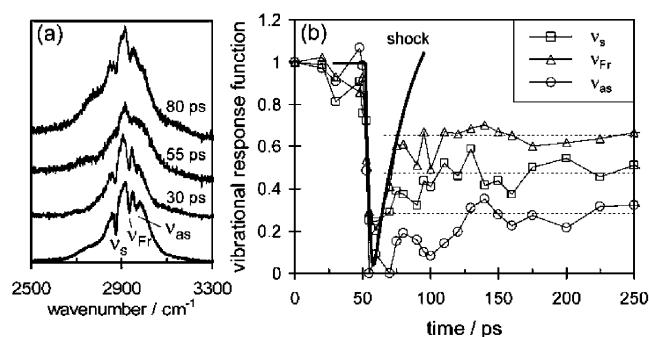


Figure 6. (a) SFG spectra of ODT/Au with shock compression. (b) Time-dependent vibrational response functions for three ODT transitions. The post-shock SFG signal recovery is incomplete. By comparison with the dashed guidelines, an ~ 30 ps process can be observed in the post-shock recovery of ν_{as} and ν_s . There is a post-shock enhancement in the ν_s/ν_{as} ratio indicating some terminal methyl groups have more upright tilt than before the shock.

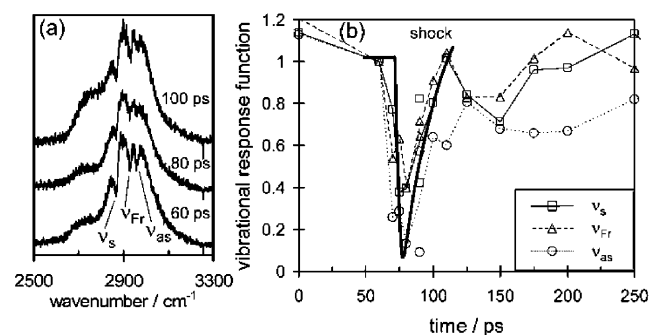


Figure 7. (a) SFG spectra of ODT/Ag with shock compression. (b) Time-dependent vibrational response functions for three ODT transitions along with the shock compression envelope. The post-shock SFG signal recovery is more elastic than with ODT/Au.

especially prominent in the ν_{as} data where its amplitude is ~ 0.3 . (3) At longer delay times, the response functions for each vibration stabilize at different levels. By definition the pre-shock response functions were all equal to unity, but after the shock, the data show proportionately more ν_s than ν_{as} . In other words the methyl species observed at longer delays has a larger ν_s/ν_{as} ratio than in the native ODT/Au structure, and hence from Figure 1b the methyl tilt must be more upright than in the native structure. This incomplete recovery and molecular reconfiguration or shape change indicate that shock compression of ODT/Au is best described as viscoelastic.

D. Shocked ODT/Ag. Figure 7 shows time-dependent data for shock compression of ODT/Ag. We did not obtain as much data as with ODT/Au, but the Ag substrate clearly results in some notable effects. The shock arrival time of ~ 75 ps, compared to 55–60 ps for Au is not notable, it is due to a slightly thicker Ag layer and a slower shock velocity⁵⁷ of ~ 2.6 km/s. The SFG signal recovery is much greater in ODT/Ag than in ODT/Au. The ν_{as} signal recovery does not evidence the ~ 30 ps process seen on Au substrates but nevertheless appears to be somewhat slower than the recovery of the other transitions. The ODT/Ag shock recovery is considerably more elastic than on Au substrates.

E. Shocked BMT/Au. As shown in Figure 8, the SFG signal in BMT disappears when the shock front arrives. The SFG signal recovers only partially, to about 0.7 of its initial value, after the shock unloads. A small-amplitude delayed post-shock recovery similar to the ~ 30 ps transient observed with alkanes on Au is also seen.

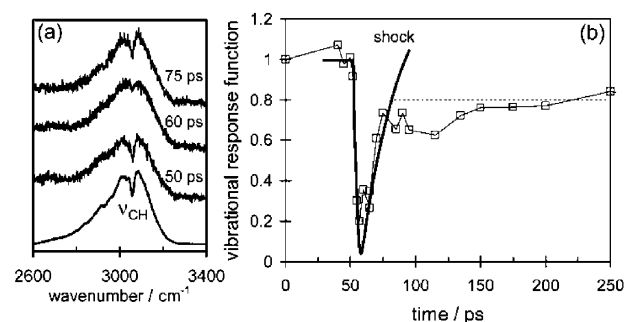


Figure 8. (a) SFG spectra of BMT/Au with shock compression. (b) Time-dependent vibrational response functions for the BMT C–H stretch transition. The post-shock SFG signal recovery is not quite complete and evidences a small-amplitude ~ 30 ps process.

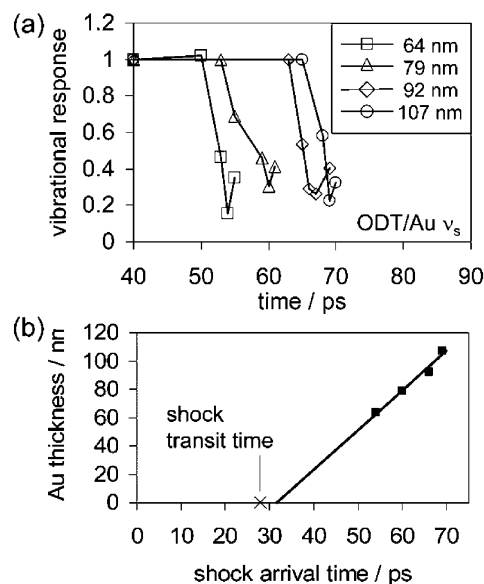


Figure 9. Experimental determination of the shock velocity in Au. The Au layer thickness was increased in ~ 10 nm increments. (a) The arrival time of the shock front is determined from the sudden drop in SFG intensity of the ν_s transition of ODT/Au. (b) The slope of the time/distance line gives a shock velocity in Au of 2.8 ± 0.3 nm/ps (km/s). Within experimental error this is equal to the small-amplitude shock velocity in Au. The intercept of ~ 32 ps results from an ~ 27 ps transit time through Cr and Ni plus an ~ 5 ps shock build up time.

F. Shock Velocity in Au. Shock arrival time data for ODT/Au with variable thickness Au layers are shown in Figure 9, probed via the vibrational response of ν_s , which is the most intense transition. Increasing the Au layer thickness (at constant Cr and Ni thickness) by ~ 10 nm increments increases the arrival time in ~ 3 ps increments. From the slope of the data in Figure 9b we obtain a shock velocity in Au of 2.8 ± 0.3 km/s, which is consistent with the small-amplitude shock velocity⁵⁷ in Au of 3.07 km/s. The best-fit line intercepts the x -axis near $t = 32$ ps. Small-amplitude shock propagation through 25 nm of Cr at 5.2 km/s and 100 nm of Ni at 4.6 km/s should require 27 ps. However, the shock must build up from rest. There is a finite time for the plasma to accelerate the metal-glass interface up to velocity and for the shock to build up,⁵⁵ so the remaining 5 (± 1) ps represents the shock build-up time.

G. Isobaric Heating. Figure 10 shows temperature-dependent spectra for ODT/Au under glycol contact fluid (bp 217 °C). Up to 110 °C the SFG CH-stretch intensities, frequencies and line widths do not change. However, slightly above 110 °C the CH stretch signals decrease and two new bands appear at lower wavenumbers. These bands are assigned to methylene ($-\text{CH}_2-$)

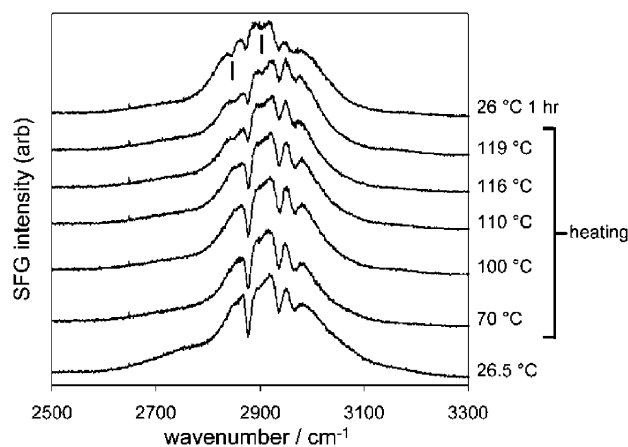


Figure 10. SFG spectra of ODT/Au under deuterated ethylene glycol contact liquid with slowly rising temperature (~ 0.5 K/min). Temperature-dependent linebroadening or shifting are not observed. Desorption begins at $T \approx 110$ °C. Methylene resonances appear at that temperature (marked by solid lines), indicating increasing disorder due to decreasing surface coverage. At $T = 119$ °C the sample was allowed to cool. The subsequent 26 °C spectrum shows that the desorption process is irreversible.

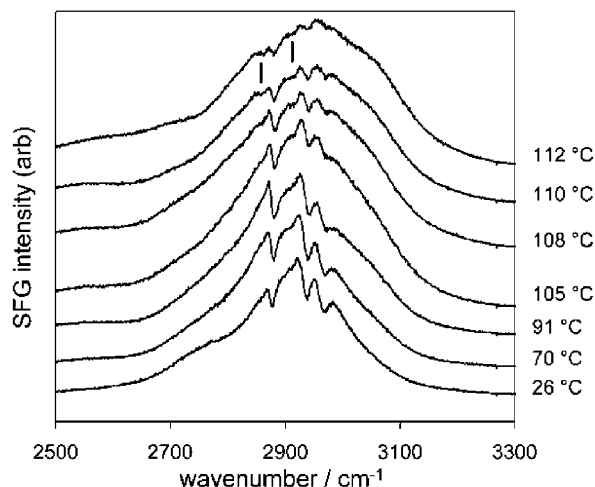


Figure 11. Rising temperature series of spectra for PDT/Au shows behavior similar to ODT/Au in Figure 10.

stretching resonances, which are also seen in SFG spectra of alkane SAMs that evidence disordering.⁴⁶ In thermal desorption experiments, the disordering presumably arises due to the lowered surface coverage. The heater current was turned off after the 119 °C spectrum was obtained, and the sample was allowed to cool to ambient temperature. The final (topmost) spectrum was taken 1 h after the return to room temperature. This spectrum shows that the loss of CH-stretch signal is irreversible, indicating that a portion of the SAM molecules desorb and get lost in the glycol layer after the temperature reaches ~ 110 °C. There is no significant difference in the temperature behavior of PDT/Au, as shown in Figure 11. In repeat experiments with ODT and PDT under glycol, the desorption temperature varied by at most ± 10 °C.

Although BMT experiments were qualitatively similar, there were two notable differences. The CH stretch intensities in BMT increased slightly with increasing temperature before desorption occurred at 110–120 °C, which Figure 1d indicates is consistent with evolution toward structures with small tilt or larger twist angles. With ODT and PDT, once desorption began it was possible to arrest the desorption process midway by shutting

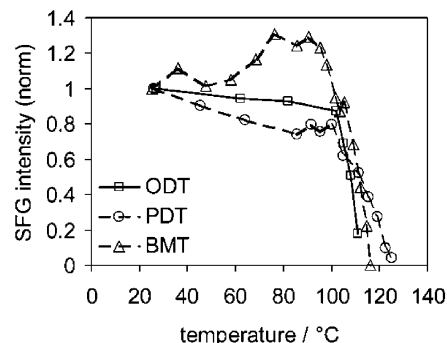


Figure 12. Comparison of the temperature response of BMT and the ν_s transitions of ODT and PDT, on Au substrates under ethylene glycol. All three molecules desorb at 110 ± 10 °C.

off the oven. However, with BMT, desorption was seemingly more autocatalytic, because once begun, it always continued to completion.

Figure 12 shows the temperature dependence of the ν_s transition of ODT/Au, ODT/Ag and the ν_2 transition for BMT/Au under glycol. Although the intensity dependences of the SFG signals for these three SAMs differ somewhat, desorption begins in all cases in the 110–120 °C temperature range.

5. Discussion

A. Temperature Dependence. We are seeing desorption temperatures in the 110–120 °C range, whereas experiments in a vacuum or inert atmospheres see desorption temperatures in the 175–225 °C range.^{52,53} Evidently the glycol contact liquid lowers the desorption temperature. Because ODT/Au, PDT/Au, and BMT/Au monolayers have quite different molecular structures and intermolecular interactions, evidently it is the Au–S anchor that is the same for all three monolayers that controls the desorption process. The glycol might destabilize the SAM anchor or stabilize the desorbed thiols.

B. Shock Front Rise Time. The sudden loss of SFG signal in < 4 ps may result from several factors: (1) the shock front rise time in the Au layer, (2) surface roughness causing a spread of shock front arrival times,⁷² (3) the intrinsic time resolution of the SFG probe, and (4) the molecular response time.

Using AFM, we have determined that the Au surface has an RMS roughness of 4 nm. This roughness averaged over the beam profile and over many laser shots should result in an ~ 1.3 ps spread in shock front arrival time.

In the SFG process, the ~ 200 fs BBIR pulse creates a vibrational coherence. The longer duration NBvis pulse interacts with the coherent polarization⁷³ to produce the SFG signal. The SFG signal is thus produced during the time interval the coherence is present. The coherence decay time constant T_2 can be estimated from the line width $\Delta\nu$ of the CH stretching resonances, using the relation, $T_2 = (\pi\nu_{1/2})^{-1}$. For SAMs with $\nu_{1/2} \approx 15$ cm^{-1} , $T_2 \sim 0.7$ ps, so the intrinsic time resolution of the SFG probe is ~ 1.4 ps.

Gahagan⁵⁴ et al. used free-surface interferometry to measure the rise time of shocks in Ni thin films having RMS roughness of 0.7 nm, under drive conditions similar to those used here. They observed transients with a 10%–90% rise time of 5.5–6.2 ps.

The usual way to combine all these finite time effects is to convolve Gaussian functions representing each contribution.⁷⁴ Using this procedure with the < 4 ps observed rise time, the 1.3 ps arrival time dispersion, and the 1.4 ps vibrational dephasing indicates the combined effects of shock front rise time and SAM material response occur within < 3.5 ps.

We do not see the two-part shock front structure that is usually expected for viscoelastic compression,¹¹ and which has been observed in ultrafast experiments on proteins and polymers with ~ 300 nm thick samples.^{12,13,75} The two-part structure results from the slightly faster velocity of the elastic compression wave, but in our thin samples there is not enough run distance for the elastic wave to cleanly separate from the shock front.

C. Shock Fall Time. The falling edge of the exponential function given by eq 13 (solid curves in Figures 5–8) is an accurate fit for the near-total recovery of PDT/Au and ODT/Ag and for the partial recovery of the other SAMs. Because the time constant associated with the falling edge is the expected time constant for shock unloading, and it is the same for all SAMs, the falling edge function should be viewed as characterizing the shock pressure decay as opposed to being a material response of the SAM.

D. Response of Alkane SAMs to Shock. *i. Shock Compression.* The SFG signal disappearance at the shock front cannot possibly be due to shock-induced desorption of the chains. The shock-induced temperature rise, estimated at ~ 50 K, is not large enough, and even if we postulated some kind of dynamic desorption process associated with the high strain rate, the SFG signal disappearance is clearly a fundamentally different process than the SFG signal loss due to thermal desorption above 120° . In the shock data we do not see methylene transitions as in Figures 10 and 11, which appear due to the disorder that ensues as chains desorb from the lattice. More significantly, in PDT/Au the SFG signal returns completely in picoseconds after the shock unloads, proving that the PDT chains did not desorb. Because PDT/Au and ODT/Au have seemingly identical thermal desorption behavior, the *post-shock SFG signal decrease* seen in ODT/Au but not in PDT/Au *cannot possibly be due to shock desorption* of the ODT. Because the chains remain adsorbed after the shock unloads, SFG signal loss at the shock front must be caused by shock-induced tilting of the methyl groups to large tilt angles near 90° .

ii. Shock Unloading. In ODT/Au, the incomplete recovery of SFG signal upon shock unloading is a clear indication of a viscoelastic process. In addition, when the shock unloads, the SFG spectra clearly evidence at least two distinct species. One species remains trapped at large methyl tilt angles during the experimental time scale, accounting for the long-term SFG signal loss. The other species undergoes an ~ 30 ps reorientation to structures with methyl groups trapped in a nearly upright stance.

The other SAMs display a basically elastic response to shock compression, although there are indications that a small portion, on the order of 10–20% of the SAM molecules undergo some kind of viscoelastic process associated with molecular deformation.

The nearly elastic response of PDT/Au observed in Figure 5 indicates that shock compression results primarily in methyl tilting and whole-chain tilting. However, in the 100–125 ps time range in Figure 5, the ν_s intensity is completely recovered whereas the ν_{as} intensity is still $\sim 15\%$ low. These data are suggestive of a transient state lasting a few tens of picoseconds where the methyl groups are on average slightly more upright than in the native configuration. However, the SFG probe cannot distinguish between a homogeneous sample with all methyl groups having identical tilts and an inhomogeneous sample with a mixture of lesser and greater tilts. Thus the data in Figure 5 could be interpreted in several ways. If the PDT response were homogeneous, then the shock dynamics of the terminal methyl should be described as an $\sim 90^\circ$ tilt behind the shock front, a prompt return during shock unloading to $\sim 45^\circ$, followed by an

~ 30 ps relaxation back to the $\sim 60^\circ$ native structure. Allowing for two species, the data cannot be fit uniquely. Generally speaking, in this case when the shock unloads, most of the molecules return to the native $\sim 60^\circ$ structure whereas a small portion briefly becomes upright before relaxing back to the native structure in ~ 30 ps.

In comparing ODT on Au and Ag, on the Ag substrate shock compression is much more elastic, and methyl groups do not get trapped in large tilt angles. This appears to be a consequence of the tighter chain packing and nearly vertical chains of ODT/Au, which apparently makes it more difficult to trap methyl groups in large tilt configurations.

In the BMT/Au experiments, we observe only one transition so our interpretation of the dynamic reorientation is more speculative. As described in Figure 1d, SFG signal loss is associated with the shock front driving the phenyl groups from the almost upright ($\theta \approx 0^\circ$) configuration down onto the substrate ($\theta \approx 90^\circ$). This can occur if the BMT molecules undergo an anti-to-gauche isomerization²⁶ around the $-S-CH_2-$ phenyl chain. The data in Figure 8 indicate that $\sim 70\%$ of BMT molecules immediately return to the native configuration, and the remainder are locked in tilted configurations. The ~ 30 ps transient might be associated with phenyl twisting in these locked tilted configurations or might be related to the unusual intensity increase near 80° C seen in Figure 12.

E. Implications for Lubrication. Static compression experiments on SAMs have been described as models for understanding lubrication.⁴⁰ The frictional force felt by a metal probe scanning over a hydrocarbon SAM in the elastic limit, where the probe moves slowly and exerts low stress, is primarily determined by the probe's interactions with the terminal $-CH_3$ groups, resulting mainly in small-amplitude methyl and chain tilts.^{39,43} It seems reasonable that our shock compression experiments, where the metal surface velocity is ~ 0.5 km/s and the strain is ~ 0.1 , can be a model for the response of lubricants at high strain rates that are found, for instance, in high-speed vehicles, disk drives and jet turbine engines that operate up to 100 000 rpm, and in the firing of shells from rifle or cannon barrels.

In these applications lubricant molecules are subjected to continual cycles of compression and expansion. It is desirable to minimize viscous effects and maximize elastic response in this cycle. Here we have observed some intriguing relationships between structure and elasticity. At the same packing density, odd chains were much more elastic than even chains (PDT/Au vs ODT/Au), but even chains could be made to respond more elastically by increasing the packing density (ODT/Au vs ODT/Ag). These considerations may provide an useful *ansatz* for the design of better lubricants for demanding applications. Similar logic might be applied in reverse to bulletproof armor where controlled viscoelastic deformation is essential to soak up a bullet's momentum.

5. Summary and Conclusions

The arrival of an ~ 1 GPa shock front causes immediate SFG signal loss in all the SAMs studied, with a time constant < 2.5 ps. SFG signal loss has also been observed in static compression experiments^{44–48} of even carbon alkane layers, where the effect was attributed to disorder or methyl tilting. The ppp measurement is sensitive to the configurational average of the molecular hyperpolarizability along the z -axis perpendicular to the substrate, so the only kinds of disorder that will lead to SFG signal loss are those which make the hyperpolarizability average to zero. We see SFG signals during the shock recovery period even

though there is disorder in the form of multiple conformational species present. As shown in Figure 1b, a wide range of azimuthal angles caused by the polycrystalline or domain structure or surface imperfections does not cause SFG signals to vanish. A tilt angle near 0° will cause ν_{as} but not ν_s to vanish. Only a tilt angle of 90° or a range of angles distributed symmetrically around a mean of 90° will cause both ν_s and ν_{as} to vanish. Similarly the static high-pressure SFG signal loss^{44–48} at ~ 10 MPa cannot be explained by disorder, nor can it be explained by SAM molecules migrating away from the compressed region, because SAM molecules do not migrate at this pressure.⁴¹ Thus we attribute SFG signal loss in both the static and dynamic compression cases to methyl tilting near 90° .

During 25 ps shock unloading, there is a dramatic difference between PDT/Au and ODT/Au. The PDT/Au behavior is simple. It recovers from compression almost elastically, presumably by simple tilting. The ODT/Au signal recovery is small, even at the longest times of ~ 1 ns, as a result of viscoelastic behavior associated with the all-trans chains losing strength, presumably by forming gauche conformers. In addition, the ODT/Au shows evidence for at least two coexisting conformers, one that remains kinetically trapped in a high tilt angle and one that relaxes into a nearly upright state in ~ 30 ps. In PDT/Au, ODT/Ag, and BMT/Au there is evidence for a minor component, say 10–20%, of viscoelastic compression. In the alkanes, the data indicate that ν_{as} takes ~ 30 ps longer to recover than ν_s , which is suggestive of a shock process involving a high tilt behind the shock front followed by at least some of the molecules taking a temporary excursion to nearly upright states before returning to the native structure. These problems will be treated in detail and given a molecular interpretation in the second paper of this series.⁷ We will also discuss⁷ why methylene SFG signals are not observed from the kinetically trapped high-tilt configurations.

An important question is how should we view the coexistence of different populations during the unloading process. There are two possibilities: the sample itself is inhomogeneous, consisting of a mixture of species, or the sample is homogeneous and it is shock compression that creates multiple species. In the former case shock compression could be viewed as a coherent perturbation on an inhomogeneous sample. The finite temperature SAMs on a rough (~ 4 nm RMS) polycrystalline surface will have thermal disorder and a complicated domain structure.³⁰ SAM molecules at domain boundaries or those temporarily in high-energy configurations the instant the shock front arrives might be more deformable than molecules in domain interiors.

In the latter case, begin by noticing that even a perfectly coherent shock front on a perfectly ordered lattice might be expected to create disorder due to stochastic fluctuations. When the shock front arrives, it would hit each molecule with a slightly different impact parameter. The compression behavior of any individual molecule might be very sensitive to the condition of its nearest neighbors, creating a disordered compressed state. But the shock front is not perfectly coherent. The actual shock front has a roughness at least as great as the substrate roughness, so the front consists of a bunch of shocklets^{56,72} that arrive at slightly different times and that impact the SAMs with a variety of impact parameters. The leading shocklets will crush domains of SAM molecules surrounded by a sea of native SAM molecules. The trailing shocklets later crush small domains of SAM molecules surrounded by a sea of crushed molecules. These earlier and later shocklets can produce different sorts of molecular deformations.

In this study we have developed a technology platform to measure the fast response of molecules to high strain rates associated with high-speed impact or high-speed moving surfaces. The combination of femtosecond shock generation pulses and ultrathin layer probing gives us the ability to turn on and to probe large-amplitude molecular deformations that cannot be photoinduced with picosecond time resolution.

We have provided a phenomenological description of the SAM shock compression process and we have clearly shown that the SAM response to shock can be dependent on both the molecular structure and on the lattice structure as determined by the metal substrate. In the next paper in this series⁷ we will provide a detailed atomistic description of SAM shock compression using molecular simulation techniques.

Acknowledgment. This material is based on work supported by U.S. Department of Energy, Division of Materials Sciences under Award No. DEFG02-91ER45439, through the Frederick Seitz Materials Research Laboratory at the University of Illinois at Urbana–Champaign and through the Stewardship Sciences Academic Alliance Program from the Carnegie-DOE Alliance Center under grant number DE-FC03-03NA00144. Additional support was provided by the National Science Foundation under award number DMR-0096466, by the U.S. Air Force Office of Scientific Research under award number F49620-03-1-0032, and by the U.S. Army Research Office under award number DAAD19-00-1-0036.

References and Notes

- (1) Dlott, D. D. *Annu. Rev. Phys. Chem.* **1999**, *50*, 251.
- (2) Schreiber, F. *Prog. Surf. Sci.* **2000**, *65*, 151.
- (3) Patterson, J.; Lagutchev, A.; Dlott, D. D. *AIP Conf. Proc.* **2004**, *706*, 1299.
- (4) Patterson, J. E.; Lagutchev, A.; Huang, W.; Dlott, D. D. *Phys. Rev. Lett.*, in press.
- (5) Zhu, X. D.; Suhr, H.; Shen, Y. R. *Phys. Rev. B* **1987**, *35*, 3047.
- (6) Harris, A. L.; Chidsey, C. E. D.; Levinos, N. J.; Loiacono, D. N. *Chem. Phys. Lett.* **1987**, *141*, 350.
- (7) Patterson, J. E.; Dlott, D. D. *J. Phys. Chem. B* **2005**, *109*, 5045.
- (8) Bain, C. D.; Troughton, E. B.; Tao, Y.-T.; Evall, J.; Whitesides, G. M.; Nuzzo, R. G. *J. Am. Chem. Soc.* **1989**, *111*, 321.
- (9) Laibinis, P. E.; Whitesides, G. M.; Allara, D. L.; Tao, Y. T.; An, P.; Nuzzo, R. G. *J. Am. Chem. Soc.* **1991**, *113*, 7152.
- (10) Zhuang, X.; Miranda, P. B.; Kim, D.; Shen, Y. R. *Phys. Rev. B: Condensed Matter Mater. Phys.* **1999**, *59*, 12632.
- (11) Graham, R. A. *Solids Under High-Pressure Shock Compression. Mechanics, Physics and Chemistry*; Springer-Verlag: New York, 1993.
- (12) Kim, H.; Hambir, S. A.; Dlott, D. D. *Phys. Rev. Lett.* **1999**, *83*, 5034.
- (13) Kim, H.; Hambir, S. A.; Dlott, D. D. *J. Phys. Chem. B* **2000**, *104*, 4239.
- (14) Voth, G. A.; Hochstrasser, R. M. *J. Phys. Chem.* **1996**, *100*, 13034.
- (15) Dlott, D. D. *Acc. Chem. Res.* **2000**, *33*, 37.
- (16) Hambir, S. A.; Franken, J.; Hare, D. E.; Chronister, E. L.; Baer, B. J.; Dlott, D. D. *J. Appl. Phys.* **1997**, *81*, 2157.
- (17) Tas, G.; Franken, J.; Hambir, S. A.; Dlott, D. D. *Phys. Rev. Lett.* **1997**, *78*, 4585.
- (18) Funk, D. J.; Moore, D. S.; Gahagan, K. T. *Phys. Rev. B* **2001**, *64*, 115114.
- (19) Tas, G.; Hambir, S. A.; Franken, J.; Hare, D. E.; Dlott, D. D. *J. Appl. Phys.* **1997**, *82*, 1080.
- (20) Funk, D. J.; Moore, D. S.; McGrane, S. D.; Gahagan, K. T.; Reho, J. H.; Suelow, S. J.; Nicholson, J.; Fisher, G. L.; Rabie, R. L. *Thin Solid Films* **2004**, *453–454*, 542.
- (21) McGrane, S. D.; Moore, D. S.; Funk, D. J. *J. Appl. Phys.* **2003**, *93*, 5063.
- (22) Bain, C. D. *J. Chem. Soc., Faraday Trans.* **1995**, *91*, 1281.
- (23) Robertson, D. H.; Brenner, D. W.; White, C. T. Microscopic simulations of complex hydrodynamic phenomena. In *High-Pressure Shock Compression of Solids III*; Davison, Shahnipoor, Eds.; Springer-Verlag: New York, 1997.
- (24) Holian, B. L. *Shock Waves* **2004**, *13*, 489.
- (25) Riele, H.; Kendall, G. K. *Langmuir* **1999**, *15*, 8867.

- (26) Jung, H. H.; Won, Y. D.; Shin, S.; Kim, K. *Langmuir* **1999**, *15*, 1147.
- (27) Kitaigorodskii, A. I. *Molecular Crystals and Molecules*; Academic Press: New York, 1973.
- (28) Bain, C. D.; Davies, P. B.; Ong, T. H.; Ward, R. N. *Langmuir* **1991**, *7*, 1563.
- (29) Richter, L. J.; Petralli-Mallow, T. P.; Stephenson, J. P. *Opt. Lett.* **1998**, *23*, 1594.
- (30) Siepmann, J. I.; McDonald, I. R. *Langmuir* **1993**, *9*, 2351.
- (31) Mao, M. Y.; Miranda, P. B.; Kim, D. S.; Shen, Y. R. *Appl. Phys. Lett.* **1999**, *75*, 3357.
- (32) Hirose, C.; Akamatsu, N.; Domen, K. *J. Chem. Phys.* **1992**, *96*, 997.
- (33) Hirose, C.; Akamatsu, N.; Domen, K. *Appl. Spectrosc.* **1992**, *46*, 1051.
- (34) Herzberg, G. *Molecular Spectra and Molecular Structure II. Infrared and Raman Spectra of Polyatomic Molecules*; Van Nostrand Reinhold: New York, 1945.
- (35) Ward, R. N.; Duffy, D. C.; Davies, P. B.; Bain, C. D. *J. Phys. Chem.* **1994**, *98*, 8536.
- (36) Salmeron, M.; Neubauer, G.; Folch, A.; Tomitori, M.; Ogletree, D. F.; Sautet, P. *Langmuir* **1993**, *9*, 3600.
- (37) Barrena, E.; Ocal, C.; Salmeron, M. *J. Chem. Phys.* **2000**, *113*, 2413.
- (38) Lee, S.; Puck, A.; Graupe, M.; Colorado, R., Jr.; Shon, Y.-S.; Lee, T. R.; Perry, S. S. *Langmuir* **2001**, *17*, 7364.
- (39) Wong, S.-S.; Takano, H.; Porter, M. D. *Anal. Chem.* **1998**, *70*, 5209.
- (40) Salmeron, M. *Tribol. Lett.* **2001**, *10*, 69.
- (41) Carpick, R. W.; Salmeron, M. *Chem. Rev.* **1997**, *97*, 1163.
- (42) Tupper, K. J.; Brenner, D. W. *Langmuir* **1994**, *10*, 2335.
- (43) Brewer, N. J.; Foster, T. T.; Leggett, G. J.; Alexander, M. R.; McAlpine, E. *J. Phys. Chem. B* **2004**, *108*, 4723.
- (44) Du, Q.; Xiao, X.-d.; Charych, D.; Wolf, F.; Frantz, P.; Shen, Y. R.; Salmeron, M. *Phys. Rev. B* **1995**, *51*, 7456.
- (45) Fraenkel, R.; Butterworth, G. E.; Bain, C. D. *J. Am. Chem. Soc.* **1998**, *120*, 203.
- (46) Beattie, D. A.; Haydock, S.; Bain, C. D. *Vibr. Spectrosc.* **2000**, *24*, 109.
- (47) Berg, O.; Klenerman, D. *J. Appl. Phys.* **2001**, *90*, 5070.
- (48) Berg, O.; Klenerman, D. *J. Am. Chem. Soc.* **2003**, *125*, 5493.
- (49) Nuzzo, R. G.; Korenic, E. M.; Dubois, L. H. *J. Chem. Phys.* **1990**, *93*, 767.
- (50) Mar, W.; Klein, M. L. *Langmuir* **1994**, *10*, 188.
- (51) Vemparala, S.; Karki, B. B.; Kalia, R. K.; Nakano, A.; Vashishta, P. *J. Chem. Phys.* **2004**, *121*, 4323.
- (52) Nishida, N.; Hara, M.; Sasabe, H.; Wolfgang, K. *Jpn. J. Appl. Phys., Pt. 1* **1996**, *35*, 5866.
- (53) Kondoh, H.; Kodama, C.; Sumida, H.; Nozoye, H. *J. Chem. Phys.* **1999**, *111*, 1175.
- (54) Gahagan, K. T.; Moore, D. S.; Funk, D. J.; Rabie, R. L.; Buelow, S. J.; Nicholson, J. W. *Phys. Rev. Lett.* **2000**, *85*, 3205.
- (55) Schoen, P. E.; Campillo, A. J. *Appl. Phys. Lett.* **1984**, *45*, 1049.
- (56) Yang, Y.; Hambir, S. A.; Dlott, D. D. *Shock Waves* **2002**, *11*, 129.
- (57) Marsh, S. P. *LASL Shock Hugoniot Data*; University of California Press: Berkeley, CA, 1980.
- (58) Hohlfield, J.; Wellershoff, S.-S.; Gädde, J.; Conrad, U.; Jähne, V.; Matthias, E. *Chem. Phys.* **2000**, *251*, 237.
- (59) Funk, D. J.; Moore, D. S.; Reho, J. H.; Gahagan, K. T.; McGrane, S. D.; Rabie, R. L. *AIP Conf. Proc.* **2002**, *620*, 1227.
- (60) Evans, R.; Badger, A. D.; Falliès, F.; Mahdih, M.; Hall, T. A.; Audebert, P.; Geindre, J.-P.; Gauthier, J.-C.; Mysyrowicz, A.; Grillon, G.; Antonetti, A. *Phys. Rev. Lett.* **1996**, *77*, 3359.
- (61) McGrane, S. D.; Moore, D. S.; Funk, D. J.; Rabie, R. L. *Appl. Phys. Lett.* **2002**, *80*, 3919.
- (62) Cagnoux, J.; Chartagnac, P.; Hereil, P.; Perez, M. *Ann. Phys. Fr.* **1987**, *12*, 451.
- (63) Millett, J. C. F.; Bourne, N. K. *J. Phys. D: Appl. Phys.* **2004**, *37*, 2901.
- (64) Zel'dovich, Y. B.; Raiser, Y. P. *Physics of Shock Waves and High-temperature Hydrodynamic Phenomena*; Academic Press: New York, 1966.
- (65) Grimsditch, M.; Rivier, N. *Appl. Phys. Lett.* **1991**, *58*, 2345.
- (66) Lee, I.-Y. S.; Hill, J. R.; Dlott, D. D. *J. Appl. Phys.* **1994**, *75*, 4975.
- (67) Litovitz, T. A.; Davis, C. M. Structural and shear relaxation in liquids. In *Physical Acoustics. Principles and Methods*; Mason, W. P., Ed.; Academic Press: New York, 1965; p 282.
- (68) Barker, L. M.; Hollenbach, R. E. *J. Appl. Phys.* **1970**, *41*, 4208.
- (69) Swegle, J. W.; Grady, D. E. *J. Appl. Phys.* **1985**, *58*, 692.
- (70) Fu, Q.; Seier, F.; Gayen, S. K.; Alfano, R. R. *Opt. Lett.* **1997**, *22*, 712.
- (71) Nishi, N.; Hobara, D.; Yamamoto, M.; Kakiuchi, T. *J. Chem. Phys.* **2003**, *118*, 1904.
- (72) Hambir, S. A.; Kim, H.; Dlott, D. D.; Frey, R. B. *J. Appl. Phys.* **2001**, *90*, 5139.
- (73) Laubereau, A.; Kaiser, W. *Rev. Mod. Phys.* **1978**, *50*, 607.
- (74) Fleming, G. R. *Chemical Applications of Ultrafast Spectroscopy*; Oxford University Press: Oxford, NY, 1986.
- (75) Kim, H.; Hambir, S.; Dlott, D. D. *Shock Waves* **2002**, *12*, 79.